Inhibition of Vibrational Energy Flow within an Aromatic Scaffold via Heavy Atom Effect

Majid Hassani,^{a,†} Christopher J. Mallon,^{a,†} Judith N. Monzy,^b Andrew J. Schmitz,^a Scott H. Brewer,^b Edward E. Fenlon,^{*b} and Matthew J. Tucker^{*a}

- a) Department of Chemistry, University of Nevada, Reno, Reno, Nevada 89557, United States
- b) Department of Chemistry, Franklin & Marshall College, Lancaster, PA 17604-3003, United States

† Authors contributed equally to the paper.

Corresponding Author

*Matthew J. Tucker, University of Nevada, Reno. Email: mtucker@unr.edu

*Edward E. Fenlon, Franklin & Marshall College, Lancaster, PA. Email:

edward.fenlon@fandm.edu

Abstract: The regulation of intramolecular vibrational energy redistribution (IVR) to influence energy flow within molecular scaffolds provides a way to steer fundamental processes of chemistry, such as chemical reactivity in proteins and design of molecular diodes. Using two-dimensional infrared (2D IR) spectroscopy, changes in intensity of vibrational cross peaks are often used to evaluate different energy transfer pathways present in small molecules. Prior 2D IR studies of para-azidobenzonitrile (PAB) demonstrated that several possible energy pathways from the N₃ to the cyano- vibrational reporters were modulated by Fermi resonance, followed by energy relaxation into the solvent. In this work, the mechanisms of IVR were hindered via the introduction of a heavy atom, selenium, into the molecular scaffold. This effectively eliminated the energy transfer pathway and resulted in the dissipation of the energy to the bath and direct dipole-dipole coupling between the two vibrational reporters. Several structural variations of the aforementioned molecular scaffold are employed to assess how each interrupted the energy transfer pathways, and evolution of 2D IR cross peaks were measured to assess changes in the

energy flow. By eliminating the energy transfer pathways through isolation of specific vibrational transitions, through-space vibrational coupling between an azido (N₃) and a selenocyanato (SeCN) probe is facilitated and observed for the first time. Thus, rectification of this molecular circuitry is accomplished through inhibition of energy flow using heavy atoms to suppress the anharmonic coupling and instead favor of a vibrational coupling pathway.

KEYWORDS (IVR, cross peaks, coupling strength)

Introduction:

After more than 25 years, two-dimensional infrared (2D IR) spectroscopy has become the premiere ultrafast technique to characterize vibrational dynamics; including drug binding events, protein folding events via transient 2D IR, energy transfer in materials, population exchange, and properties of ion channels in cell membranes.²⁻¹² 2D IR uniquely separates the homogeneous and inhomogeneous contributions to absorption lineshapes, revealing the phenomenon of spectral diffusion. The temporal dynamics of spectral diffusion can be measured through center line slope of the contours in the 2D IR spectra. The behavior of the CLS matches that of the frequencyfrequency correlation functions (FFCF), which reveal the localized solvent dynamics in the heterogeneous solutions, which play an important role in reactivity. 13-16 Another attractive feature of 2D IR spectroscopy comes from its ability to determine the types of interactions between multiple vibrational transitions within a molecular scaffold via the appearance and behaviour of cross peaks. For example, vibrational coupling, i.e. mechanical and/or dipole-dipole coupling, 4, 17, ¹⁸ results in cross peaks in the 2D IR spectrum at the earliest waiting times and then decay over time.^{2, 4, 19-21} On the other hand, cross-peaks that become more intense as a function of waiting time are indicative of population exchange or vibrational energy relaxation (VER).^{1, 22} If the VER entails several vibrational modes becoming delocalized within a molecular system to overlap in

their vibrational motion, it is referred to as intramolecular vibrational energy redistribution (IVR). The thermal energy propagation is delayed because the energy absorbed by one vibration must flow through the molecular scaffold until it finally reaches another vibration. ²³⁻²⁶ Theoretical ²⁷⁻³² and experimental studies of VER have discussed different factors influencing the rates of thermal energy flow, relative directions of heat flow, and characteristics of diffusive/ballistic transport. ^{23,} ³³⁻³⁹ Oftentimes, multiple dark states are involved in the energy transfer pathways that creates challenges in predicting the energy flow within the molecule and determining the rate. ²⁴ However, several methods have been developed to successfully design molecules that decouple certain modes to guide the preferred route of energy flow. ^{1, 22, 24, 40}

The ability to guide VER within a molecular system would enhance many chemical processes, including synthetic chemistry, ^{24, 39-42} the development of molecular electronics. ^{33, 34, 43-45} It can also influence the three dimensional structures of molecular systems. ^{6, 26, 46, 47} Furthermore, protein functionality is significantly influenced by VER affecting hydrogen bonding, ⁴⁸ secondary and tertiary structure formation, ³² and allosteric communication. ^{49, 50} Thus, guiding VER within a molecule provides a way to influence these processes in a desirable way or even inhibit them if necessary.

Recently, 2D IR studies have investigated the necessary elements for guiding energy flow within molecular scaffolds and factors that influence the overall pathway. Some studies involving transition metals have suggested that heavy atoms can influence transfer efficiency, direction of relaxation, and the contribution of solvent on IVR. 35, 51, 52 2D IR studies by Zheng and co-workers have reported the influence on the rates of intermolecular energy transfer over different distances and orientations between vibrations of a wide array of molecular systems. 24, 39, 40, 43, 44, 46 Rubtsov and co-workers have developed relaxation-assisted two-dimensional infrared spectroscopy (RA

2DIR)²³ to evaluate the energy transfer rates between various vibrational mode pairs over a variety of distances.^{26, 53-55} Energy transfer rates were found to be most dependent on bond length^{44, 47, 54} and temperature.⁵⁵

Recently, Tucker and co-workers uncovered a method to predict the most probable energy transfer pathway through coupled dark modes via the assessment of third order coupling parameters.¹ In these studies, para-azidobenzonitrile (PAB) and para-methylazidobenzonitrile (PAMB) were shown to exhibit several possible energy pathways from the N₃ to the cyanovibrational reporters facilitated by Fermi resonant modes (Figure 1).

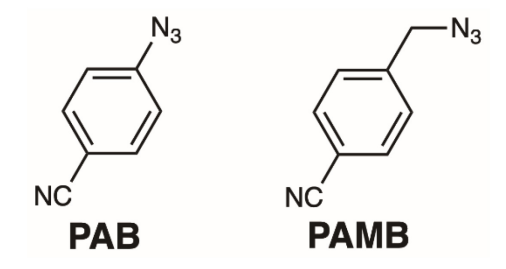


Figure 1. Structure of para-azidobenzonitrile (PAB) and para-methylazidobenzonitrile (PAMB).

In this study, several structural variations of the molecular scaffold are employed to interrupt these energy transfer pathways, and the evolution of 2D IR cross peaks were measured to assess changes in the energy flow. By isolating specific vibrational transitions and thus hindering the energy transfer pathway, dipole-dipole coupling was facilitated, allowing direct coupling to be detected between N₃ and weak SeCN vibrational modes for the first time. Comparison between experimentally determined vibrational coupling and theoretical analysis of coupling strengths for the studied molecular systems was assessed. Differences in energy of the vibrational transitions, transition dipole strengths, and angle between the dipoles are addressed in terms of the observed couplings. Thus, the ability of heavy atoms to suppress energy transfer pathways and thereby influence the flow of energy in molecular circuitry is effectively demonstrated.

Materials and Methods:

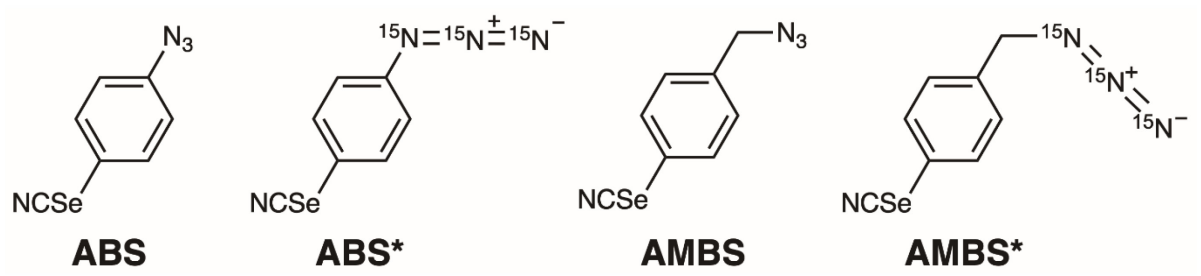


Figure 2. Structures of 4-azidobenzoselenocyanate (ABS), triple-¹⁵N-labeled 4-azidobenzoselenocyanate (ABS*), 4-azidomethylbenzoselenocyanate (AMBS), and triple-15N-labeled 4-azidomethylbenzoselenocyanate (AMBS*).

Sample Preparation: The vibrational coupling between N₃ and SeCN vibrational reporters was studied using 4-azidobenzoselenocyanate (ABS), triple-¹⁵N-labeled 4-azidobenzoselenocyanate (ABS*), 4-azidomethylbenzoselenocyanate (AMBS), and triple-¹⁵N-labeled 4-azidomethylbenzoselenocyanate (AMBS*), see Figure 2. Complete synthetic details are given in supporting information.

The same synthetic route was used to prepare ABS and ABS*, as illustrated for ABS* in Scheme 1. Electrophilic aromatic substitution of ¹⁵N-labeled aniline (1*) by triselenium dicyanide, generated in situ from selenium dioxide and malononitrile, produced labeled selenocyanate 2* in modest yield.⁵⁶ The triple-labeled N₃ isotopologue of ABS was obtained by diazonium ion formation with ¹⁵N labeled sodium nitrite followed by the addition of triple-labeled sodium azide. This two-step sequence gave a 52% yield of ABS*. The unlabeled synthesis gave an 87% yield of selenocyanate 2 and a 34% yield of ABS.

The synthesis of AMBS was accomplished by the four-step, two-pot sequence outlined in Scheme 2. Aniline 3 was diazotized with acidic sodium nitrite followed the addition of potassium

selenocyanate to provide intermediate 4 in modest yield. Conversion of the alcohol of 4 to the mesylate leaving group followed by an S_N2 reaction with azide anion provided AMBS in 15% yield after purification. The same method was used to synthesize AMBS*, but triple-¹⁵N-labeled sodium azide was used to provide the product in 28% yield.

Linear and 2D IR Methods: Solutions of 30-40 mM ABS, AMBS, ABS*, and AMBS* in tetrahydrofuran (THF) were prepared for both 2D IR and FTIR experiments. The FTIR and 2D IR samples were placed in a Harrick sample cell with CaF₂ windows and a pathlength of 56 µm for ABS and AMBS and a 100 µm pathlength for ABS* and AMBS*. Linear infrared spectra were measured using a Nicolet 6700 FTIR. To determine the full width at half maximum (FWHM), each transition was fit to a Gaussian profile, $y = A \cdot e^{-4 \ln(2)(x-x_c)^2/w^2}$.

2D IR experiments were performed in the boxCARs geometry⁵⁷⁻⁵⁹ with Fourier-transform 80-fs pulses with a central wavelength ranging from 4650-4750 nm depending on the sample. Three laser pulses, each with an energy ~1 μ J, with wave vectors k_1 , k_2 , and k_3 , were incident on the samples to generate a signal in the direction k_{sig} =- k_1 + k_2 + k_3 with time-ordering of 123 (rephasing) and 213 (nonrephasing). To acquire absorptive spectra, the rephasing and nonrephasing 2D frequency spectra were properly phased and combined.⁵⁸ The waiting time, T, between the second and third pulse was varied from 0 to 6 ps in order to measure the dynamics observed in the 2D line shapes. After appropriate Fourier transforms along the coherence, τ , and detection, t, axes, the 2D IR spectra are plotted ω_{τ} vs. ω_{t} . The vibrational relaxation times, T_{10} ,

were estimated from the decay of the on-diagonal signal strengths of the v=0 \rightarrow v=1 transition in the 2D IR spectrum at different waiting times and fitted to an exponential decay, $A = A_0 e^{-T/T_{10}}$.

Coupling values are obtained from the experimental 2D IR data using the equation $\beta_{1,2}^{(ex)} = \frac{|E_2 - E_1|}{2\sqrt{1 + \frac{\Delta}{\Delta_{12}}}}$. Here, E_1 and E_2 are the observed energies of the coupled transitions, Δ_{12} is the observed

off-diagonal anharmonicity between the peak positions of the positive and negative contours of the cross peaks, and Δ is the geometric average of the anharmonicities of the fundamental transitions, defined by the difference between the peak positions of the positive and negative contours of the diagonal peaks. This equation comes from the perturbative treatment of the anharmonicity on a system of two coupled harmonic oscillators, to first order.²

Computational Methods: Both Gaussian09 and Gaussian16⁶⁰ were used to perform density functional theory (DFT) calculations of ABS, AMBS, ABS*, and AMBS* at the B3LYP/6-31+G (d,p) level of theory. An implicit solvation model of THF was used through all calculations with the self-consistent reaction field (SCRF) in the conducting polarizable continuum model (CPCM). Optimizations were followed by harmonic frequency calculations to obtain frequency and energy data. Anharmonic frequency calculations were performed to identify the possible Fermi resonances that appear in the infrared spectra.

The normal mode coordinates obtained from the frequency calculations were used to determine the coupling constant between the N₃ and SeCN reporters using the finite difference method (FDM).⁶¹ The coupling values in this approach were obtained after perturbing the optimized structure by a small amount (0.03 times the oscillation amplitude in Å) along the N₃ and SeCN normal modes. Single point energy calculations were performed after perturbation and used to calculate the vibrational coupling through the second derivative of the energy with respect to

both normal modes. The second-order central difference scheme was utilized to calculate the mixed second derivative of the potential energy surface.

The dihedral angle along the C-N bond connecting the phenyl group with the N₃ reporter in ABS was rotated from 90° to 450° to map out the potential energy surface along this degree of freedom. Likewise, the C-N bond connecting the methyl group with the N₃ reporter in AMBS was rotated from 0° to 360°. The resulting structures at each step of the rotation were allowed to relax to a minimum energy with the dihedral angle fixed. The relative energies were then plotted as a function of dihedral angle. A sampling of structures near the local minima, defined to be approximately within the thermal distribution at room temperature (~0.59 kcal/mol), were then used to calculate the average angles and distances between the SeCN and N₃ dipoles as well as their dipole moment strengths and coupling constants obtained in FDM calculations.

Results and Discussion:

Linear IR Spectra of ABS and AMBS. FTIR measurements were conducted on ABS and AMBS in THF. The linear IR spectrum of ABS in THF exhibits three transitions observed at 2092, 2128, and 2154 cm⁻¹, as shown in Figure 3A. For the spectrum of ABS, the asymmetric stretch of the N₃ transition appears at 2092 cm⁻¹, and the SeCN stretch is located at 2154 cm⁻¹. The third transition centered at 2128 cm⁻¹ arises from a Fermi resonance, an 'accidental' resonance of a combination band consisting of two ring modes with the fundamental N₃ transition, which has been reported in previous work of similar molecular scaffolds. ^{1,62-65} The linear IR spectrum of AMBS in THF also had three distinct transitions located at 2098, 2130 and 2154 cm⁻¹ corresponding to the N₃, Fermi, and SeCN transitions, respectively. As a result of adding one methylene group between the benzene ring and the azide, a 6 cm⁻¹ blue-shift was observed in the vibrational frequency of the N₃ transition and a negligible shift in the Fermi transitions. A shift in frequency of the N₃ transition

closer to the Fermi transition likely indicates a slight decoupling of the ring modes from the N₃ transition. The coupled vibrational frequencies are expected to be more separated from the original uncoupled frequencies holding to a simple bilinear coupling model. Thus, some decoupling has occurred. On the other hand, the SeCN stretching frequency remains independent of the molecular structure due to the heavy atom effect.^{66, 67}

The spectral profile of AMBS shows a weak transition observed around 2130 cm⁻¹ which was detected in the linear IR spectrum. The identity of this transition is further confirmed by cross peaks detected in the 2D IR spectrum (discussed below) due to the anharmonic (Fermi) coupling. However, the intensity of this Fermi resonance is much weaker than ABS because of separation of the benzene ring from the N₃ group using one carbon atom.⁶⁸ This reduction of the anharmonic coupling was observed in our earlier work on PAB and PAMB.¹ It was found in the same work that this loss of anharmonic coupling between the N₃ group with the lower energy ring modes through the Fermi resonance leads to a much slower energy transfer within the vibrational scaffold and slightly alters the transfer pathway.¹

The calculated FWHM for ABS, as obtained from fitting to Gaussian line shapes was 19.3, 18.6, and 9.1 cm⁻¹ for N₃, Fermi, and SeCN transitions, respectively. The linewidths of the two fundamental transitions obtained for AMBS were similar to that of ABS, exhibiting a FWHM of 23.9 and 9.1 cm⁻¹ for the N₃ and SeCN transitions, respectively. However,

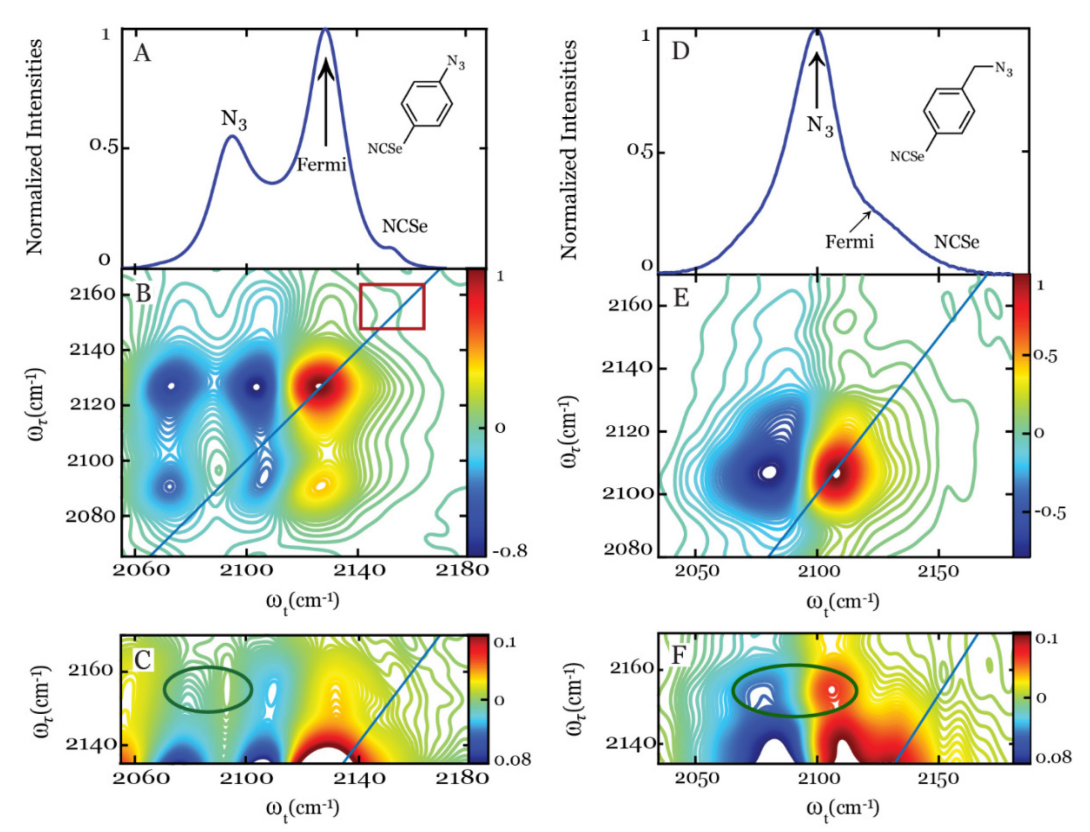


Figure 3. FTIR spectra of (A) ABS and (D) AMBS in THF and absorptive 2D IR spectra of (B) ABS and (E) AMBS in THF at T = 800 fs. Figures C and F show the cross peak region expanded of Figures B and E, respectively.

the FWHM of the Fermi transition broadened to 29.31 cm⁻¹ in AMBS is likely due to a broader distribution of modes coupling to the fundamental transition.⁶⁸ The broader distribution of coupled dark ring modes will have less intensity as a result of the decreased mixing within the bilinear coupling matrix. The experimental IR intensity ratio between the fundamental N₃ transition and Fermi resonance was 1:1.79 for ABS compared to 1:0.22 for AMBS. It is clear that the addition of a methylene between the benzene ring and azide reporter causes the strength of Fermi resonance to decrease as the azide reporter is brought into resonance with different combination bands of the benzene ring. Furthermore, these differences in spectral profile can easily be replicated by varying the strength of the anharmonic coupling in the coupling matrix by a few wavenumbers.

Table 1. Experimental and calculated transition frequencies for the N₃, SeCN, and Fermi resonances.

| | Experimental (cm ⁻¹) | | | Calculated (cm ⁻¹) | | |
|--------|----------------------------------|------------------|-----------------|--------------------------------|------------------|--------------------------|
| Sample | ω_{N_3} | ω_{Fermi} | ω_{SeCN} | ω_{N_3} | ω_{Fermi} | ω_{SeCN} |
| ABS | 2092 | 2128 | 2154 | 2119 | 2125 | 2154 |
| AMBS | 2099 | 2130 | 2154 | 2101 | 2113 | 2154 |
| ABS* | 2037 | 2070 | 2154 | 2055 | 2084 | 2154 |
| AMBS* | 2031 | 2055 | 2154 | 2038 | 2084 | 2154 |

Computations. Ab initio density functional theory (DFT) calculations of anharmonic frequencies were performed after geometry optimization in order to confirm the identity of the N₃ and SeCN modes as well as determine the possible anharmonic modes that contribute to the Fermi resonance. The results of the DFT calculations confirmed the identities of the two transitions in the spectral region corresponding to the N₃ asymmetric stretch as well as the SeCN stretch based on the values of their relative vibrational frequencies. A correction factor of 0.9675 was applied to match the experimental and calculated SeCN vibrational frequency at 2154 cm⁻¹. A summary of the calculated and experimental vibrational frequencies of both vibrational reporters as well as the suspected Fermi resonances (combination bands of low frequency ring modes) are given in Table 1. The SeCN vibration in ABS, AMBS, ABS*, and AMBS* were all predicted to be at the same frequency which agrees with the experimental results. The calculated N₃ asymmetric stretch frequencies were 2119 cm⁻¹, 2101 cm⁻¹, 2055 cm⁻¹, and 2038 cm⁻¹ for ABS, AMBS, ABS*, and AMBS*, respectively. It should be noted that the modes involving the Fermi resonances were not determined solely based on resonance with fundamental N₃ frequency. Instead, the Fermi resonances were determined from anharmonic calculations by the combination band with the highest predicted intensity that was close to the region in which the Fermi resonance was observed experimentally.

2D IR Spectroscopy. 2D IR spectra of ABS and AMBS at early waiting times are shown in Figures 3B and 3E, respectively. Akin to the linear IR spectrum, the $N_3 v = 0 \rightarrow v = 1$ transitions appear along the diagonal at $\omega_t = \omega_\tau = 2092$ cm⁻¹ and $\omega_t = \omega_\tau = 2107$ cm⁻¹ for ABS and AMBS, respectively. The negative contours red-shifted along the ω_t axis represent $v = 1 \rightarrow v = 2$ transitions result from the anharmonic nature of the oscillations. The diagonal anharmonicities of the N_3 transitions for ABS and AMBS are approximately 26.4 ± 0.4 and 20 ± 6 cm⁻¹, respectively. The vibrational lifetime for the N_3 transition was measured to be $\sim 0.28 \pm 0.04$ ps (Figure S4). The rapid population decay is a result of the fast energy transfer to the ring modes, as mentioned above.

Another diagonal transition corresponding to the Fermi resonance seen in the linear IR spectra for ABS is located at $\omega_t = \omega_\tau = 2130$ cm⁻¹. A strong cross peak, $\omega_t = 2134$ cm⁻¹ and $\omega_\tau = 2091$ cm⁻¹, decreases in intensity as a function of waiting time in the 2D IR spectrum of ABS. This is attributed to strong anharmonic coupling, ~12.4 cm⁻¹, between the N₃ and Fermi transitions, as calculated using the coupling equation above. Although the ¹³C NMR spectrum indicates the presence of SeCN, it should be noted that the expected transition is not observed in the 2D IR spectrum of ABS at $\omega_t = \omega_\tau = 2154$ cm⁻¹ due to its extremely weak transition dipole strength, ~0.06 D.⁶⁹ However, the presence of this weak transition is revealed by the off-diagonal cross peaks representing coupling between the N₃ and the SeCN transitions, located at $\omega_t = 2154$ cm⁻¹ and $\omega_\tau = 2091$ cm⁻¹ (shown by green ovals in Figure 3C). Upon careful examination of the spectrum, a small elongation of the positive-going transition toward higher energy is found along ω_t , highlighted by the red rectangle in Figure 3B. This rectangle indicates the suspected location of SeCN transition. To verify its location, the vibrational transition of SeCN oscillator is clearly shown for another isotopically labelled scaffold, documented in SI (Figure S6).

The mechanism of coupling is very different from the prior scaffold, PAB, investigated for its thermal energy flow, i.e. energy transfer. In the PAB scaffold, the thermal energy flow occurred from the N₃ transition to several anharmonically coupled modes eventually reaching the nitrile group. The current scaffold, ABS, shows that this energy pathway has been interrupted by the presence of the Se atom, taking advantage of the well-known heavy atom effect, which isolates the vibration preventing rapid damping and energy leakage to the rest of the molecule. This change in mechanism of vibrational dynamics is indicated by lack of growth observed for the off-diagonal cross peak between the SeCN and N₃ transitions (see Figures S1 and S2 in Supporting Information).

Instead, the 2D IR spectrum of ABS demonstrates for the first time the presence of dipole-dipole coupling between weak (almost undetected) SeCN and the strong N₃ transitions. This observation further suggests that the intensity mixing that occurs in the coupling matrix provides a way to observe modes with significantly weak transition dipole strength, such as SeCN. These extremely weak modes need only to be coupled to another mode with much stronger dipole strength, such as N₃. A dipole-dipole coupling strength, ~21 cm⁻¹, was determined between the N₃ and SeCN modes from cross peaks for the estimated distance of ~6.13 Å from the computed structure. This ability to hinder the thermal pathway provides an avenue to change the flow of energy within a molecule, which has utility in developing molecular circuitry. Also, this methodology allows measurement of distances with these vibrational reporters in other larger scaffold where energy transfer can be problematic.

To further evaluate the ability to suppress energy transfer pathways, the AMBS scaffold was compared to PAMB which contained at least two thermal energy pathways from the N₃ to the CN transitions. Similar to PAMB, the AMBS 2D IR spectrum displays a significant decrease in

the Fermi resonance bands, $\omega_t = \omega_\tau = 2130 \text{ cm}^{-1}$, and their off-diagonal cross peaks, $\omega_t = 2107 \text{ cm}^{-1}$ and $\omega_\tau = 2130 \text{ cm}^{-1}$, indicating that the first part of the energy transfer pathway is intact but with a reduced rate. The experimental 2D IR results also show that the coupling between the azido and Fermi transitions reduce by ~1-2 cm⁻¹ in AMBS as compared with ABS. The rate of energy transfer is affected by both this reduction and the addition of the carbon atom between the benzene ring and the N₃ group. The vibrational lifetime was measured for the N₃ transition to be ~0.89 \pm 0.06 ps (Figure S4). This population decay is 3.2 times longer than the ABS scaffold due to reduction of anharmonic coupling and less damping of the energy.

As observed in ABS, all the off-diagonal cross peaks in the spectrum decay as function of waiting time from the earliest times (see Supporting Information, Figures S1 and S2), indicating the loss of energy transfer to the SeCN transition. Once again, the Se atom was able to interrupt the multiple thermal transfer pathways between the N₃ and CN transitions in the prior PAB scaffold. Despite the slight decrease in coupling strength between N₃ to Fermi transitions mentioned above, the thermal pathway between the N₃ and Fermi transitions is still open as indicated by the delocalization of vibration shown in the energy density calculation (computed and shown below). Analysis of the cross peaks seen between the SeCN and N₃ transitions in AMBS revealed a similar coupling strength, ~19.6 cm⁻¹, to that observed for ABS over the estimated distance of 6.9 Å from the computed structure. It should be noted that even though the structural distance is slightly larger, the dipole moment orientation is expected to be more favorable leading to the similarity in vibrational coupling (see computation results below).

Isotopic Labeled Samples. Another strategy to suppress the energy transfer pathways is to decrease the Fermi resonance, or strong anharmonic coupling, present in the scaffold via isotopic labelling.⁶² With this in mind, two more compounds containing triple-¹⁵N isotopic labelling of the

N₃ group, ABS* and AMBS*, were synthesized and measured. In these labelled compounds the N₃ vibrational frequency is shifted thereby reducing the overlap of the nearly resonant dark ring modes. This isotopic labeling resulted in a red shift of the fundamental frequency by 55 cm⁻¹ and 67 cm⁻¹ for ABS* (2037 cm⁻¹) and AMBS* (2031 cm⁻¹), respectively. Fermi resonance transitions were also observed centered at 2070 cm⁻¹ and 2055 cm⁻¹ for ABS* and AMBS*, respectively. (See Figure 4). It should be noted that a significant drop in intensity is also observed when compared to the unlabeled compounds mentioned in Figure 3. The lack of energetic overlap of the combination bands of the ring modes and the fundamental N₃ stretch causes the coupling constant to decrease by a few wavenumbers, ~2-3 cm⁻¹. Akin to the previous compounds, the vibrational frequency of SeCN transitions remained unchanged at 2154 cm⁻¹ for both ABS* and AMBS*.

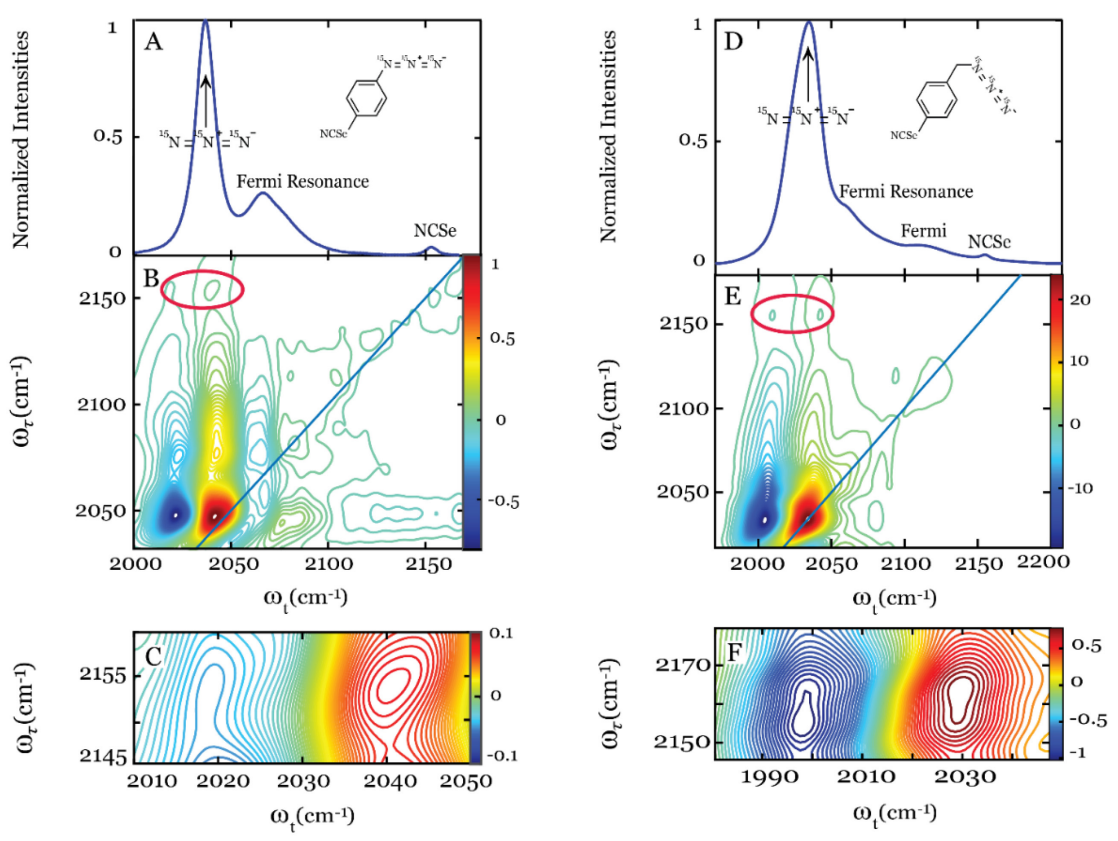


Figure 4. FTIR spectra of (A) ABS* and (D) AMBS* in THF and absorptive 2D IR spectra of (B) ABS* and E) AMBS* in THF at T = 200 fs. Figures C and F show the cross peak region expanded of Figures B and E, respectively.

For ABS*, a FWHM of 13.8 cm⁻¹ was observed for N₃ transition showing a decrease of ~ 6 cm⁻¹ when compared to the unlabeled ABS. On the other hand, the Azide-transition of AMBS* has a FWHM of 26 cm⁻¹, which is more comparable to the bandwidth of the unlabeled AMBS compound. The Fermi resonance bandwidth significantly increased in both cases. The FWHM of the Fermi resonances increased by 12 cm⁻¹ in ABS* and 21 cm⁻¹ in AMBS* when compared to the unlabeled samples. The increased width is somewhat expected due to the lower intensity of the transitions and the reduced coupling. The IR intensity ratios between Fermi and N₃ were found to be 0.26:1 and 0.18:1 in ABS* and AMBS*, respectively. This follows our expectations that the intensities ratio between the N₃ and Fermi transitions decreases as a function of the isotopic labeling and reduction of the anharmonic coupling. It should be noted that an additional broadened vibrational transition is detected at 2107 cm⁻¹. This transition is likely due to additional Fermi resonance with different combination modes.⁶⁸ As expected, the FWHM of SeCN transition remains unaffected by isotopic labeling.

2D IR measurements of ABS* showed a single strong transition along the diagonal observed at $\omega_t = \omega_\tau = 2040~\text{cm}^{-1}$ identified as the N₃ transition. The anharmonicity of this transition for ABS* is approximately 19.2 cm⁻¹. ABS* showed a much weaker Fermi resonance at $\omega_t = \omega_\tau = 2066~\text{cm}^{-1}$ compared to ABS. Although the shifted N₃ transition decoupled the original dark ring modes, the shifted N₃ frequency became resonant with different combination modes of the ring, as computed in the DFT anharmonic frequencies calculations. The density of states of the ring modes are very rich in this region of the spectrum. As a result of this anharmonic coupling, two sets of strong cross peaks were observed on either side of the diagonal at $\omega_t = 2040~\text{cm}^{-1}$, $\omega_\tau = 2080~\text{cm}^{-1}$ as well as $\omega_t = 2082~\text{cm}^{-1}$, $\omega_\tau = 2040~\text{cm}^{-1}$. The anharmonic coupling strength, ~10.6 cm⁻¹ (Table S1), again decreased slightly due to less overlap with these new combination bands

of the ring. The vibrational lifetime was also measured for the N_3 transition to be $\sim 1.56 \pm 0.17$ ps (Figure S4). This population decay is ~ 5 -6 times longer than the ABS scaffold most likely due to reduced anharmonic coupling via isotopic labeling of the N_3 group. A table of the population relaxations and cross peak decays are included in the supporting information (Table S2).

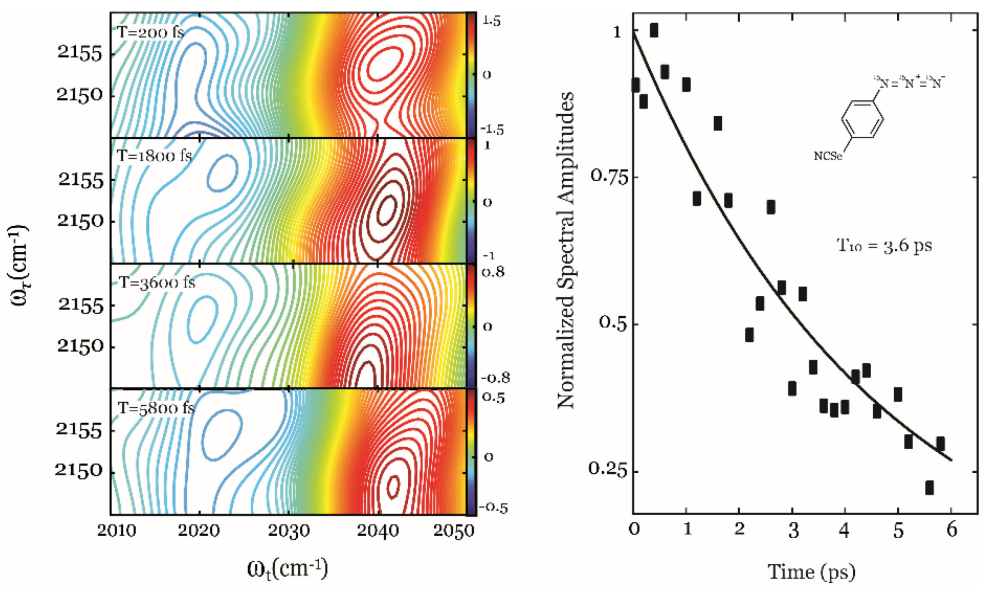


Figure 5. (left) Off-diagonal cross-peak region and (right) decay of cross peak intensity as a function of waiting time of ABS*.

Furthermore, a larger dipolar coupling, ~33 cm⁻¹, was observed between the SeCN and the labeled N₃ group, likely due to more isolation of the vibrational oscillations involved. These cross peaks are observed at $\{\omega_t, \omega_\tau\} = \{2041, 2154\}$ cm⁻¹ in ABS*, highlighted by the red ovals in Figure 4B. Figure 5 shows the intensity decay of cross peaks as a function of waiting time, T. The decay of these cross peaks, indicative of anharmonically coupled modes, yields further evidence that the energy transfer pathway has been blocked. The time constant observed for the cross peak decay is 3.6 ± 0.9 ps, limited by vibrational lifetime of the N₃ transition of 1.56 ± 0.17 ps. A summary of the population relaxations and cross peak decays are included in the supporting information (Table S2).

Similarly, the N₃ transition for AMBS* was shifted to $\omega_t = \omega_\tau = 2031 \text{ cm}^{-1}$ as a result of isotopic labeling to the N₃ nitrogens, with a diagonal anharmonicity of 29.7 cm⁻¹. As before, the

shift in N₃ frequency did not completely remove the Fermi resonances, but instead different anharmonically coupled combination bands were observed at $\omega_t = \omega_\tau = 2107 \text{ cm}^{-1}$. The coupling strength, ~10.4 cm⁻¹, was determined from the corresponding cross peaks at $\{\omega_t, \omega_\tau\} = \{2031, 2107\} \text{ cm}^{-1}$. The value was reduced for the unlabeled samples because of the decrease in resonance with the N₃ fundamental stretching transition. Another cross peak was observed at $\{\omega_t, \omega_\tau\} = \{2031, 2154\} \text{ cm}^{-1}$ representing the coupling between the N₃ and the SeCN transitions. The measured coupling strength, ~38 cm⁻¹, showed a two-fold increase compared to the unlabeled AMBS.

The isotopic labelling was able to reduce the degree of anharmonic coupling between the N₃ and the dark ring modes. This reduction of the anharmonic coupling was sufficient to observe a significant increase in the vibrational coupling between the N₃ and SeCN transitions. However, due to the resonance with other combination bands of rings modes, the N₃ transition remained delocalized. Overall, based on the reduced anharmonic coupling caused by the shifted N₃ transitions, the decrease in intensity ratios of the N₃ to Fermi- transition, and the gradual increase of vibrational lifetimes of the N₃ transition, a systematic trend was observed, showing increases in the dipolar coupling of the two fundamental transitions.

Coupling Analysis and Calculations. A scan of the dihedral angle between the benzene ring and the N₃ group was performed through a full rotation about the C-N bond (shown in Figure 6) for both ABS and AMBS. At each angle, the geometry was allowed to relax to a minimum while the dihedral angle remained fixed. Since DFT methods do not consider isotopic effects on the total energy, the minimized structures of ABS* and AMBS* were the same as those for ABS and AMBS. The energy dependence about the dihedral angle resulted in two energetic minima along the potential energy surface (PES) for ABS, located at 180° and 360°, as expected based on

conjugation of the p-orbital on the internal N atom and the benzene ring. On the other hand, three local minima along the PES, located at 66°, 178°, and 290°, were observed for AMBS (Figure 6).

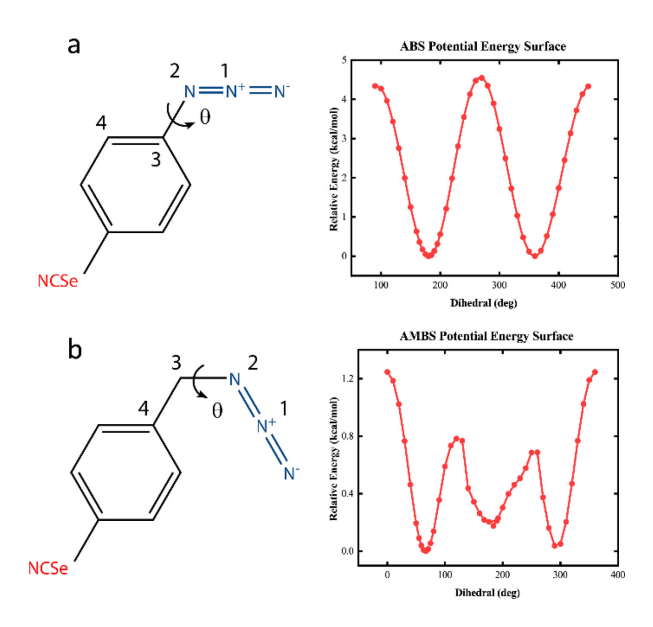


Figure 6. (a) ABS and (b) AMBS molecules with the labeled atoms that represent the dihedral angle of interest, and the calculated relative energies at different dihedral angles for (c) ABS and (d) AMBS.

Note that all three minima of the PES for AMBS exist within the thermal equilibrium, defined to be below 0.59 kcal/mol at 298 K. The dipole moments, distances, orientation, and couplings were then calculated at each dihedral angle within the thermal distribution for ABS, AMBS, ABS*, and AMBS*. Since the PES for ABS was symmetric, only a sampling of the region between 160° and 200° is reported. The same region was used for ABS*. The average values found in the regions from 55° to 75° (region 1) and 160° to 200° (region 2) are reported for AMBS and AMBS* their corresponding thermal distribution.

The average dipole moment of the N_3 and SeCN transitions of ABS were found to be 0.547 \pm 0.004 and 0.114 \pm 0.002 D, respectively. The calculated average distance between dipoles for ABS was 6.12 ± 0.001 Å with angle between dipoles of $101.2^{\circ} \pm 10.5^{\circ}$. The corresponding values found in AMBS for minima 1 was 0.429 ± 0.009 D and $0.118 \pm 0.8x10^{-6}$ D for N_3 and SeCN transitions, respectively. The values in minima 2 for AMBS were found to be 0.481 ± 0.008 D and

 0.118 ± 0.001 D for N₃ and SeCN, respectively. The average distances between dipoles for AMBS were 6.93 ± 0.005 Å and 6.94 ± 0.01 Å with the corresponding angle between dipoles found to be $36.0^{\circ} \pm 0.8^{\circ}$ and $68.8^{\circ} \pm 7.4^{\circ}$ in regions 1 and 2, respectively. Similar to ABS, the average dipole moments for ABS* were found to be 0.538 D and 0.117 D for the N₃ and SeCN transitions, respectively, with an angle between dipoles of 105.6° . The dipole moments for AMBS* in minima 1 were found to be 0.408 D and 0.117 D for the N₃ and SeCN transitions, respectively. The values in minima 2 for AMBS* were found to be 0.460 D and 0.117 D for the N₃ and SeCN transitions, respectively. The average angle between dipoles were found to be $35.2^{\circ} \pm 1.1^{\circ}$ and $67.8^{\circ} \pm 1.4^{\circ}$ in regions 1 and 2, respectively. Overall, the dipole strengths and the distances between the dipoles do not vary much between the different samples. However, the orientation and angle between the dipoles is significantly different between the samples leading to differences in their vibrational coupling.

The transition dipole coupling (TDC) theory was utilized to predict the interactions between the N_3 and SeCN transitions based on the calculated geometries and dipole moments. The average TDC coupling magnitude for ABS and ABS* was found to be $\sim 1.55~\rm cm^{-1}$. The average TDC coupling value in AMBS and AMBS* was $0.4~\rm cm^{-1}$ over both regions 1 and 2. Interestingly, the correct trend to lower coupling strength is observed for ABS compared to AMBS. However, the TDC model severely underestimated the measured experimental couplings between the two transitions. It is not unexpected since the TDC model is known to fail when the oscillation amplitude is comparable to the distance between the dipoles. $^{18, 61, 70}$ To accurately capture the coupling between the vibrational reporters, a more sophisticated model must be utilized.

Thus, the Finite difference method (FDM) was employed to quantify the coupling from DFT calculations. This analytic coupling scheme is performed by estimating the second derivative of the PES with respect to the displacements in local modes of vibration:

$$\beta_{12} = \frac{\partial^2 V}{\partial Q_1 \partial Q_2}.$$

The central difference scheme was employed, and single-point energy calculations were performed after displacing the atoms in the molecules by 0.03 times the oscillation amplitude. The resulting coupling values were then averaged over small regions of the dihedral angle within the thermal equilibrium. The average FDM coupling strengths were also calculated in the same regions. The average value of the coupling was found to be 18.3 cm⁻¹ in ABS and 9.8 cm⁻¹ over both regions 1 and 2 of AMBS. As with TDC, the decrease in the vibrational coupling is accurately reproduced between ABS (~21 cm⁻¹) and AMBS (~19.6 cm⁻¹). The absolute magnitude of the coupling is accurate to ~87% for ABS and only ~50% for AMBS. The inaccuracies in the reproducibility likely stem from the multi-mode coupling that is present experimentally, i.e. the combination of Fermi coupling and dipolar coupling. For example, the delocalization of the N₃ transition (shown below) can play an important role. The coupling matrix would be more complex generating different values than a traditional bilinear coupling model. The couplings strengths were not calculated for ABS* and AMBS* because the required DFT total energies do not consider isotopic effects.

Each fundamental oscillation was investigated to determine how isolated the vibrational transition was from the rest of the molecule. Transition densities were calculated as the difference in electron density from equilibrium after a displacement of +0.03 Å. This perturbation was used to investigate the dependence of the transition density with the displacement from equilibrium. The resulting density plots are shown with an iso value of 0.003 esu/bohr in Figures 7 for ABS

and AMBS. From these plots, it is apparent that the SeCN transition is well localized to the CN atoms in both ABS and AMBS. However, the N₃ transition is somewhat delocalized in both ABS and AMBS given that the transition density extends between the three nitrogen atoms of the azido group. The delocalization of the N₃ mode in both compounds indicates that the energy transfer pathway is still active between the N₃ transition and the benzene ring.

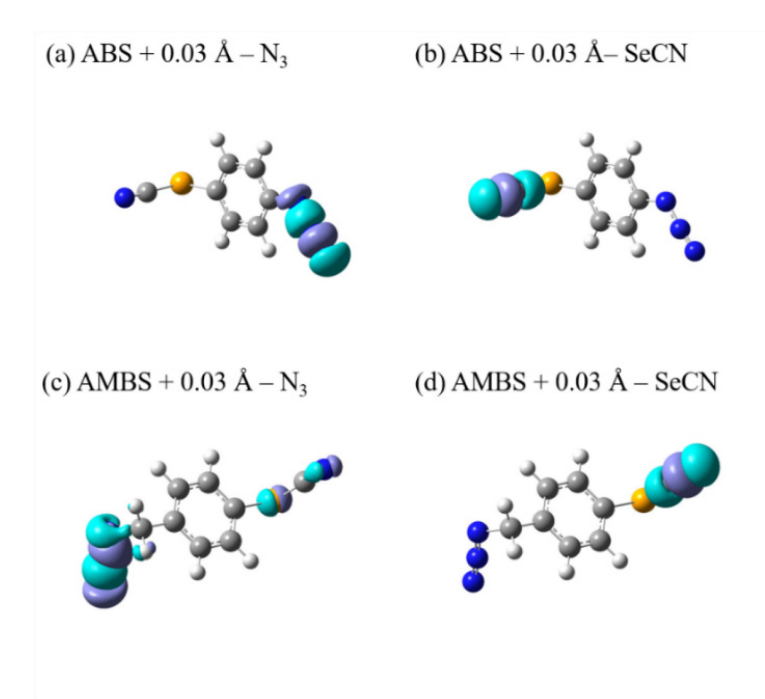


Figure 7. Calculated transition densities of the N_3 and SeCN transitions of ABS (a,b) and AMBS (c,d) after perturbating the minimized structures ± 0.03 Å along the normal mode coordinates.

CONCLUSIONS:

Several structural variations of the molecular scaffold were employed attempting to interrupt the thermal energy transfer pathways between the CN and N₃ moieties found in a prior study. To assess these thermal energy pathways, an evolution of 2D IR cross peaks were utilized to measure the changes in the energy flow across the molecule. The energy transfer pathway between the N₃ transition and the benzene ring remained intact even despite isotopic labeling. The shifting of the vibrational frequencies via isotopic labelling could not remove the overlap with the

ring modes due to the large density of states. However, taking advantage of heavy atom effect provided by a selenium atom, the cyano vibrational transition was isolated from the ring modes. By eliminating the anharmonic coupling to the ring, the energy transfer pathway through the entire molecule (N₃ to SeCN) was thus hindered and dipole-dipole coupling was facilitated. Thus, vibrational coupling of a N₃/SeCN probe pair was observed for the first time. Also, a method is developed to measure distances with these vibrational reporters in other larger scaffold where energy transfer can be problematic and prevent such determination.

The coupling strength is directly related to the molecular structure, i.e. the angle between the dipoles and the distance between transitions. However, TDC does not accurately reproduce the magnitude of the experimental observed coupling due to the similarity of the transition length compared to the distance between probes. The FDM was then utilized to compute theoretical coupling values between the N₃ and SeCN vibrational reporters from single-point energy DFT calculations. The obtained coupling strengths from this method were in reasonable agreement with those obtained experimentally for ABS and AMBS. Coupling strengths of ABS* and AMBS* were not calculated because DFT total energies do not consider isotopic effects. Thus, the potential for rectification of this molecular circuitry is accomplished through inhibition of energy flow using heavy atoms. This study is thus a proof of the principle that heavy atoms can sufficiently isolate specific vibrational modes leading to the suppression of some transfer pathways (IVR) in favor of others (vibrational coupling).

Supplementary Material.

The supplementary material contains details of the synthesis, determination of coupling strengths, decays of cross peaks, vibrational lifetime decays, and polarization-controlled pump probe.

AUTHOR INFORMATION

Notes

The authors declare no competing financial interests.

ACKNOWLEDGMENT:

M.J.T., C.J.M. and M.H. acknowledge the NSF for the financial support of this work through CHE-

2102275. E.E.F. and S.H.B. acknowledge NIH for funding this work through R15GM093330.

References:

- ¹ A. J. Schmitz *et al.*, J Phys Chem A **123** (2019) 10571.
- ² P. Hamm et al., Proc. Natl. Acad. Sci. U. S. A. **96** (1999) 2036.
- ³ F. Chalyavi et al., Angewandte Chemie International Edition **57** (2018) 7528.
- ⁴ A. J. Schmitz et al., J. Phys. Chem. B **120** (2016) 9387.
- ⁵ H. T. Kratochvil *et al.*, Science **353** (2016) 1040.
- ⁶ I. V. Rubtsov, Acc Chem Res **42** (2009) 1385.
- ⁷ F. A. Chalyavi, O.; Weiner, J. M.; Monzy, J. N.; Schmitz, A. J.; Nguyen, J. K.; Fenlon, E. E.; Brewer,
- S. H.; Odoh S. O.; Tucker, M. J., The Journal of Chemical Physics 152 (2020)
- ⁸ F. Chalyavi, A. J. Schmitz, and M. J. Tucker, J Phys Chem Lett **11** (2020) 832.
- ⁹ M. T. Zanni, Proc. Natl. Acad. Sci. U. S. A. **113** (2016) 4890.
- ¹⁰ N. H. C. Lewis et al., J Phys Chem C **124** (2020) 3470.
- ¹¹ J. S. Ostrander et al., J. Phys. Chem. B **121** (2017) 1352.
- ¹² R. Yuan, and M. D. Fayer, J. Phys. Chem. B **123** (2019) 7628.
- ¹³ S. Bagchi *et al.*, J. Phys. Chem. B **113** (2009) 8412.
- ¹⁴ J. Zheng et al., Science **309** (2005) 1338.
- ¹⁵ F. Chalyavi, D. G. Hogle, and M. J. Tucker, J. Phys. Chem. B **121** (2017) 6380.
- ¹⁶ M. C. Asplund, M. T. Zanni, and R. M. Hochstrasser, Proc. Natl. Acad. Sci. U. S. A. **97** (2000) 8219.
- ¹⁷ L. P. DeFlores *et al.*, J. Phys. Chem. B **110** (2006) 18973.
- ¹⁸ A. T. Krummel, and M. T. Zanni, J. Phys. Chem. B **110** (2006) 13991.
- ¹⁹ A. M. Woys et al., J Am Chem Soc **134** (2012) 19118.
- ²⁰ P. Hamm, and M. Zanni, *Concepts and Methods of 2D Infrared Spectroscopy* (Cambridge University Press, 2012),
- ²¹ A. Remorino, and R. M. Hochstrasser, Acc Chem Res **45** (2012) 1896.
- ²² A. Ghosh, M. J. Tucker, and R. M. Hochstrasser, J Phys Chem A **115** (2011) 9731.
- ²³ N. I. Rubtsova, and I. V. Rubtsov, in *Annual Review of Physical Chemistry*, edited by M. A. Johnson, and T. J. Martinez2015), pp. 717.
- ²⁴ H. Bian *et al.*, J Chem Phys **133** (2010) 034505.
- ²⁵ X. He *et al.*, J. Phys. Chem. B **121** (2017) 9411.

- ²⁶ D. V. Kurochkin, S. R. Naraharisetty, and I. V. Rubtsov, Proc. Natl. Acad. Sci. U. S. A. **104** (2007) 14209.
- ²⁷ D. M. Leitner, Annu Rev Phys Chem **59** (2008) 233.
- ²⁸ D. M. Leitner, and H. D. Pandey, Ann Phys-Berlin **527** (2015) 601.
- ²⁹ H. D. Pandey, and D. M. Leitner, Chem Phys **482** (2017) 81.
- ³⁰ D. M. Leitner, and H. D. Pandey, J Chem Phys **143** (2015) 144301.
- ³¹ H. Fujisaki, and G. Stock, J Chem Phys **129**, 134110 (2008) 134110.
- ³² P. H. Nguyen, S. M. Park, and G. Stock, J Chem Phys **132**, 025102 (2010) 025102.
- ³³ B. C. Pein, and D. D. Dlott, J Phys Chem A **118** (2014) 965.
- ³⁴ B. C. Pein, Y. Sun, and D. D. Dlott, J Phys Chem A **117** (2013) 6066.
- ³⁵ X. Dong *et al.*, J. Phys. Chem. B **122** (2018) 1296.
- ³⁶ F. Yang, J. Zhao, and J. Wang, J. Phys. Chem. B **120** (2016) 1304.
- ³⁷ I. V. Rubtsov, and R. M. Hochstrasser, Journal of Physical Chemistry B **106** (2002) 9165.
- ³⁸ J. C. Owrutsky, D. Raftery, and R. M. Hochstrasser, Annu Rev Phys Chem **45** (1994) 519.
- ³⁹ H. Bian, W. Zhao, and J. Zheng, J Chem Phys **131** (2009) 124501.
- ⁴⁰ H. T. Bian et al., Journal of Chemical Physics **132** (2010)
- ⁴¹ S. Rafiq et al., Chem-Us **5** (2019) 402.
- ⁴² D. M. Leitner, Adv Phys **64** (2015) 445.
- ⁴³ H. T. Bian *et al.*, P Natl Acad Sci USA **108** (2011) 4737.
- ⁴⁴ Z. Lin *et al.*, Phys Chem Chem Phys **14** (2012) 10445.
- ⁴⁵ V. M. Kasyanenko *et al.*, J Chem Phys **131** (2009) 154508.
- ⁴⁶ H. Chen *et al.*, J. Phys. Chem. B **119** (2015) 4333.
- ⁴⁷ J. Li *et al.*, J. Phys. Chem. B **117** (2013) 4274.
- ⁴⁸ E. H. Backus *et al.*, J. Phys. Chem. B **112** (2008) 15487.
- ⁴⁹ H. M. Muller-Werkmeister, and J. Bredenbeck, Phys Chem Chem Phys **16** (2014) 3261.
- ⁵⁰ H. M. Muller-Werkmeister et al., Angew Chem Int Ed Engl **52** (2013) 6214.
- ⁵¹ S. Kaziannis *et al.*, Phys Chem Chem Phys **13** (2011) 10295.
- ⁵² M. Delor et al., J. Phys. Chem. B **118** (2014) 11781.
- ⁵³ V. M. Kasyanenko *et al.*, J. Phys. Chem. B **115** (2011) 11063.
- ⁵⁴ S. R. Naraharisetty, V. M. Kasyanenko, and I. V. Rubtsov, J Chem Phys **128** (2008) 104502.
- ⁵⁵ N. I. Rubtsova *et al.*, J. Phys. Chem. B **118** (2014) 8381.
- ⁵⁶ A. V. Kachanov *et al.*, Tetrahedron Lett **45** (2004) 4461.
- ⁵⁷ Y. S. Kim, and R. M. Hochstrasser, J. Phys. Chem. B **109** (2005) 6884.
- ⁵⁸ Y. S. Kim, J. Wang, and R. M. Hochstrasser, J. Phys. Chem. B **109** (2005) 7511.
- ⁵⁹ C. Fang, and R. M. Hochstrasser, J. Phys. Chem. B **109** (2005) 18652.
- ⁶⁰ M. J. Frisch et al., Wallingford, CT, 2016).
- ⁶¹ A. Moran, and S. Mukamel, P Natl Acad Sci USA **101** (2004) 506.
- ⁶² J. S. Lipkin *et al.*, J Phys Chem Lett **2011** (2011) 1672.
- ⁶³ J. Zhang et al., J. Phys. Chem. B **122** (2018) 8122.
- ⁶⁴ M. Maj *et al.*, Phys Chem Chem Phys **17** (2015) 11770.
- ⁶⁵ X. S. Gai *et al.*, Phys Chem Chem Phys **13** (2011) 5926.
- ⁶⁶ F. Chalyavi *et al.*, Phys Chem Chem Phys **22** (2020) 18007.
- ⁶⁷ D. E. Levin *et al.*, RSC Adv **43** (2016) 36231.
- ⁶⁸ C. Varner *et al.*, Chem Phys **512** (2018) 20.

 ⁶⁹ S. M. Fica-Contreras *et al.*, J. Phys. Chem. B **125** (2021) 8907.
⁷⁰ A. T. Krummel, and M. T. Zanni, Journal of Physical Chemistry B **112** (2008) 1336.